






Ab initio electronic factors of the *A* and *B* hyperfine structure constants for the $5s^25p6s\ ^1,^3P_1^o$ states in Sn I

Asimina Papoulia ^{1,2,*}, Sacha Schiffmann ^{2,3,*}, Jacek Bieroń ⁴, Gediminas Gaigalas⁵, Michel Godefroid ³, Zoltán Harman⁶, Per Jönsson¹, Natalia S. Oreshkina ^{6,§}, Pekka Pyykkö⁷ and Ilya I. Tupitsyn⁸

¹Department of Materials Science and Applied Mathematics, Malmö University, SE-20506 Malmö, Sweden

²Division of Mathematical Physics, Department of Physics, Lund University, SE-22100 Lund, Sweden

³Spectroscopy, Quantum Chemistry and Atmospheric Remote Sensing (SQUARES), CP160/09, Université libre de Bruxelles (ULB), 1050 Brussels, Belgium

⁴Instytut Fizyki Teoretycznej, Uniwersytet Jagielloński, ul. prof. Stanisława Łojasiewicza 11, Kraków, Poland

⁵Institute of Theoretical Physics and Astronomy, Vilnius University, Saulėtekio av. 3, LT-10222, Vilnius, Lithuania

⁶Max Planck Institute for Nuclear Physics, Saupfercheckweg 1, 69117 Heidelberg, Germany

⁷Department of Chemistry, University of Helsinki, PO Box 55 (A. I. Virtasen aukio 1), FIN-00014 Helsinki, Finland

⁸Department of Physics, St. Petersburg State University, 198504 St. Petersburg, Russia



(Received 22 July 2020; revised 18 December 2020; accepted 11 January 2021; published 12 February 2021)

Large-scale *ab initio* calculations of the electronic contribution to the electric quadrupole hyperfine constant *B* were performed for the $5s^25p6s\ ^1,^3P_1^o$ excited states of neutral tin. To probe the sensitivity of *B* to different electron correlation effects, three sets of variational multiconfiguration Dirac-Hartree-Fock and relativistic configuration interaction calculations employing different strategies were carried out. In addition, a fourth set of calculations was based on the configuration interaction Dirac-Fock-Sturm theory. For the $5s^25p6s\ ^1P_1^o$ state, the final value of $B/Q = 703(50)$ MHz/b differs by 0.4% from the one recently used by Yordanov *et al.* [*Commun. Phys.* **3**, 107 (2020)] to extract the nuclear quadrupole moments *Q* for tin isotopes in the range $^{117-131}\text{Sn}$ from collinear laser spectroscopy measurements. Efforts were made to provide a realistic theoretical uncertainty for the final B/Q value of the $5s^25p6s\ ^1P_1^o$ state based on statistical principles and on correlation with the electronic contribution to the magnetic dipole hyperfine constant *A*.

DOI: [10.1103/PhysRevA.103.022815](https://doi.org/10.1103/PhysRevA.103.022815)

I. INTRODUCTION

The uninterrupted developments of computational methodologies [1–3], together with the growing computational resources at the disposal of atomic physicists, have increased tremendously the accuracy of atomic structure calculations in the past decades [4–11]. Theoretical predictions of atomic properties have, therefore, become efficient tools to support the corresponding experimental measurements. This is exemplified by the recent precision measurements of hyperfine structures [12–15]. In atoms, the hyperfine structure splittings are, to the lowest orders, described by the magnetic dipole (M1) and electric quadrupole (E2) hyperfine coupling constants *A* and *B*, respectively. The *A* constant arises from the interaction of the nuclear magnetic dipole moment μ_I , with the magnetic field generated by the electrons at the site of the nucleus. At the same time, the *B* constant is the result of the interaction between the nuclear electric quadrupole moment *Q* and the electric field gradient (EFG), which reflects the electronic charge distribution in the vicinity of the nucleus.

The quadrupole moments *Q* are important characteristics of nuclei that provide a measure of the deviation of the nuclear charge distribution from a spherical shape. In general, they can be determined from nuclear, atomic, molecular, or solid-state spectroscopies, such as high-resolution laser spectroscopy [12], muonic or pionic x-ray spectroscopy [16], nuclear magnetic resonance (NMR) [17,18], nuclear quadrupole resonance (NQR) [19,20], Mössbauer measurements [21,22], or perturbed angular correlation (PAC) of nuclei passing thin foils [23,24]. Most of these techniques require to evaluate the electronic contribution B/Q to the E2 hyperfine constant. The accuracy of the extracted *Q* values is, therefore, strongly affected by the uncertainties in the calculations of this electronic property. Three compilations of available *Q* values are provided by Raghavan [25], Stone [26], and Pyykkö [27].

In this work, we focus on tin, with an atomic number $Z = 50$. All proton shells at this magic number are closed, but the incomplete neutron shells can still induce a *Q* with quadratic dependence on the neutron number *N*, which will not become magic until the ^{132}Sn isotope, with $N = 82$ and nuclear spin $I = 0$. The nuclear trends of the *Q* moments among 8 isotopes in the range $^{117-131}\text{Sn}$, which is below the doubly magic isotope, have just recently been published by Yordanov *et al.* [12]. The $Q(\text{Sn})$ values given in Ref. [12] were based on measured atomic hyperfine structures for odd-*N* isotopes. More specifically, they were obtained by combining

*These authors contributed equally to this work.

†asimina.papoulia@mau.se

‡saschiff@ulb.ac.be

§natalia.oreshkina@mpi-hd.mpg.de

the measured B constant in the $[\text{Pd}]5s^25p6s\ ^1P_1^0$ state¹ of the neutral atom (Sn I), for each isotope, with the calculated electronic contribution B/Q . The B/Q value resulted from the three independent multiconfiguration Dirac-Hartree-Fock (MCDHF) and relativistic configuration interaction (RCI) calculations [28,29] reported in this work. The relative accuracy of the calculated B/Q is of the order of 7%, while the accuracy of the measured B constants varies, depending on the isotope, between 1.5% for ^{131}Sn and 33% for ^{125}Sn , as also reflected in Table 1 of Ref. [12]. As a result, the accuracy of the evaluated $Q(\text{Sn})$ values ranges between 7% and 34%.

In Ref. [12], the focus was on the description of the experimental methods and the interpretation of the nuclear physics results. The aim of this work is to provide the details of the employed MCDHF-RCI computational methodologies for evaluating the electronic contribution B/Q for the $5s^25p6s\ ^1\text{P}_1^0$ excited states in Sn I. Additionally, the inferred B/Q values from averaging the individual results of the three independent series of MCDHF-RCI calculations are validated by a fourth set of calculations, based on the configuration interaction Dirac-Fock-Sturmian (CI-DFS) theory [30–34]. After taking into account the results from this new set of calculations, the final B/Q value for the $^1P_1^0$ state is slightly shifted from 706(50) MHz/b in Ref. [12]² to 703(50) MHz/b in this work. Aside from the E2 hyperfine electronic contributions, the electronic parts A_I/μ_I of the M1 hyperfine constants were also calculated for the same $^1\text{P}_1^0$ states. The correlation between the M1 and E2 hyperfine structures was used as a tool to evaluate the theoretical uncertainty of the B/Q value for the $^1P_1^0$ state.

Due to the sensitivity of the hyperfine electronic factors to different electron correlation effects, one must often perform more than one set of calculations, which follow different computational strategies and correlation models, to be in a position to evaluate the accuracy of the results [35]. That being the case, a detailed description of the employed computational strategies is deemed necessary to better understand the contributions from the different correlation effects in systems with similar electronic structure and to, eventually, advance the current computational methods and computer codes.

In Sec. II, the underlying theories of the MCDHF-RCI and CI-DFS methods are briefly described. In the same section, the forms of the M1 and E2 hyperfine interaction operators that are used to compute the electronic contributions to the hyperfine structure constants A and B are given. In Sec. III, the computational details and results from the four independent sets of calculations are discussed. These results are combined in Sec. IV to provide the final B/Q value for the $^1P_1^0$ state and its associated theoretical uncertainty. The resulting B/Q value is, then, used in Sec. V to reextract the nuclear quadrupole moment Q of the ^{119}Sn isotope. Finally, our concluding remarks are presented in Sec. VI.

¹[Pd] is used, for brevity, to indicate the 46-electron palladiumlike core and will be omitted in the following.

²Although the electronic contribution B/Q is proportional to the computed EFG value (see also Sec. II C), one should note that, in Ref. [12], the quantities EFG and B/Q are used interchangeably.

II. THEORY

A. MCDHF-RCI multiconfiguration methods

The principles of the MCDHF-RCI method are fully discussed in, e.g., the book by Grant [28] and the review article by Froese Fischer *et al.* [29]. With this section, we provide the reader with a short introduction of the main concepts, as implemented in the GRASP2K [36] and GRASP2018 [1] computer packages that were used to perform the calculations presented in Sec. III A.

In the relativistic framework, the MCDHF method describes an atomic state function (ASF), $\Psi(\gamma\Pi JM)$, as an expansion over a set of jj -coupled relativistic CSFs, $\Phi_\mu(\gamma_\mu\Pi JM)$, characterized by the parity Π , the total electronic angular momentum J , and the projection quantum numbers M , i.e.,

$$\Psi(\gamma\Pi JM) = \sum_{\mu=1}^{N_{\text{CSFs}}} c_\mu \Phi_\mu(\gamma_\mu\Pi JM), \quad (1)$$

$$\text{where } \sum_{\mu=1}^{N_{\text{CSFs}}} c_\mu^2 = 1.$$

The CSFs are antisymmetrized many-electron functions built from one-electron Dirac orbitals. In the expression above, γ_μ represents the configuration, the angular momentum coupling tree, and other quantum numbers that are necessary to uniquely describe each CSF.

In the MCDHF method, the radial parts of the Dirac orbitals and the mixing coefficients c_μ are computed in a self-consistent field (SCF) procedure. The SCF radial equations to be iteratively solved are derived from the application of the variational principle on a weighted Dirac-Coulomb energy functional of the targeted atomic states according to the extended optimal level scheme (EOL) [37]. The angular integrations needed for the construction of the energy functional are based on the second quantization formalism in the coupled tensorial form [38,39].

The MCDHF calculations provide the one-electron orbital basis, which, in the subsequent relativistic configuration interaction (RCI) calculations, is used to determine the final wave functions $\Psi(\gamma\Pi JM)$ by diagonalizing the interaction matrix. At this RCI step, the transverse photon interaction, which reduces to the Breit interaction at the low-frequency limit, and the leading quantum electrodynamic (QED) corrections are added to the Dirac-Coulomb Hamiltonian (see Refs. [40,41] for more details). In the RCI calculations, the atomic-state expansions are usually augmented by CSFs that capture additional electron correlation effects.

B. CI-DFS method

The detailed description of the CI-DFS method can be found in Refs. [30–34]. We highlight hereafter the most important underlying theoretical background.

Dirac-Fock-Sturm orbitals of a general type φ_j can be obtained as the solutions of the following eigenvalue problem:

$$(h_D - \varepsilon)\varphi_j = \lambda_j W(r)\varphi_j, \quad (2)$$

where h_D is the one-electron Dirac Hamiltonian, $W(r)$ is a weight function, ε is a reference energy, and λ_j is the eigenvalue. Following Refs. [30,31], we adopt the weight function

$$W(r) = \left[\frac{1 - \exp[-(\beta r)^2]}{(\beta r)^2} \right], \quad (3)$$

where the parameter β is chosen to speed up the convergence of the Sturmian series. The set of Sturmian eigenfunctions forms a discrete and complete orthonormalized basis set of one-electron wave functions with weight $W(r)$, which are used as virtual orbitals in subsequent calculations.

The next step is the construction of an orthonormalized set of one-electron wave functions from the solutions of the DF equations in the DFS orbital basis. One-electron wave functions that were previously obtained using the DF method stay intact, whereas the virtual Sturmian orbitals are modified to be eigenfunctions of the DF operator and they can, thus, be used for the construction of determinants in the configuration interaction (CI) method.

C. Hyperfine structure

The hyperfine structure contribution to the Hamiltonian is represented by a multipole expansion

$$H_{\text{hfs}} = \sum_{k \geq 1} \mathbf{T}^{(k)} \cdot \mathbf{M}^{(k)}, \quad (4)$$

where $\mathbf{T}^{(k)}$ and $\mathbf{M}^{(k)}$ are spherical tensor operators of rank k in the electronic and nuclear spaces, respectively. The $k = 1$ and 2 terms represent the M1 and E2 interactions. In the fully relativistic approach, the electronic contributions are obtained from the expectation values of the irreducible spherical tensor operators [42,43]

$$\mathbf{T}^{(1)} = -i\alpha \sum_{j=1}^{N_e} (\boldsymbol{\alpha}_j \cdot \mathbf{l}_j) \mathbf{C}^{(1)}(j) \frac{1}{r_j^2} \quad (5)$$

and

$$\mathbf{T}^{(2)} = - \sum_{j=1}^{N_e} \mathbf{C}^{(2)}(j) \frac{1}{r_j^3}, \quad (6)$$

where \mathbf{l} is the electronic orbital angular momentum and $\mathbf{C}^{(1)}$ and $\mathbf{C}^{(2)}$ are the renormalized spherical harmonics of rank 1 and 2, respectively.

The hyperfine structure splitting for a state J is normally expressed in terms of the A and B hyperfine constants, respectively, given by

$$A = \frac{\mu_I}{I} \frac{1}{\sqrt{J(J+1)(2J+1)}} \langle \Psi | \mathbf{T}^{(1)} | \Psi \rangle \quad (7)$$

and

$$B = 2Q \sqrt{\frac{J(2J-1)}{(J+1)(2J+1)(2J+3)}} \langle \Psi | \mathbf{T}^{(2)} | \Psi \rangle \quad (8)$$

In the equations above, we adopted the definition of the reduced matrix element, which is compatible with the Wigner-Eckart theorem of Edmonds [44], as used in most of the

atomic physics textbooks. For later use, we introduce the A_{el} and B_{el} electronic factors of the hyperfine constants, i.e.,

$$A_{\text{el}} = AI/\mu_I \text{ [MHz}/\mu_N], \quad (9)$$

$$B_{\text{el}} = B/Q \text{ [MHz/b]}, \quad (10)$$

assuming that A and B are expressed in MHz, μ_I in nuclear magnetons (μ_N) and Q in barns (b). Given the electronic factors, the hyperfine constants A and B can easily be evaluated for a given isotope characterized by the (μ_I, I, Q) set of nuclear parameters.

Due to the extended magnetic and charge distributions of the nucleus, respectively, resulting in the Bohr-Weisskopf (BW) and the Breit-Rosenthal-Crawford-Schawlow (BR) corrections, the quantity A_{el} is not purely electronic. A change in these nuclear structure properties for different isotopes contributes to the hyperfine anomaly, which is particularly important for extracting magnetic dipole moments from experimental measurements [45]. However, the BW effect was estimated, in the CI-DFS calculations, to be $<0.1\%$ for both considered states (see also Sec. III B). Additionally, as shown in Ref. [12], the hyperfine anomaly along the tin isotope sequence remains small. An analogous effect takes place when computing the quantity B_{el} and it was also estimated to be $<0.1\%$ for the states in question (see Sec. III B for details). In all four independent sets of calculations presented in this work, the BR correction was included by using the Fermi model approximation for the nuclear charge distribution. It should be mentioned that the B_{el} factor is proportional to the EFG, also denoted q . Expressing the latter in a_0^{-3} and B_{el} in MHz/b, the conversion factor should be

$$B_{\text{el}}[\text{MHz/b}] = 234.9646 q [a_0^{-3}] \quad (11)$$

where the latter is often given in theoretical works [46].

III. CALCULATIONS

In this section, we report the computational details of the three independent sets of MCDHF-RCI calculations and the fourth set of CI-DFS calculations that were carried out. The respective values of the computed isotope-independent hyperfine structure constants A_{el} and B_{el} are, then, presented and analyzed. Experimental data (see, e.g., Ref. [12]) and state compositions indicate that the hyperfine structure in Sn I is characterized by a substantial E2 splitting in the $^1P_1^o$ state and a large M1 splitting in the $^3P_1^o$ state. For this reason, in what follows, we only display the $A_{\text{el}}[{}^3P_1^o]$ and $B_{\text{el}}[{}^1P_1^o]$ values. Nonetheless, the computed $A_{\text{el}}[{}^1P_1^o]$ and $B_{\text{el}}[{}^3P_1^o]$ values are still used (see Sec. III A 4) for evaluating the ratios of the A_{el} and B_{el} factors between the two states and for further comparing with the corresponding experimental values deduced in Ref. [12].

A. MCDHF-RCI calculations

The accuracy of the MCDHF-RCI multiconfiguration calculations relies on how the atomic-state expansions of Eq. (1) are built. A first approximation of the atomic states is obtained by performing an MCDHF calculation on expansions that are built from one, or more, reference configurations. These configurations are associated with the targeted atomic states

TABLE I. The sequence of layers of correlation orbitals optimized in the S-MR3-MCDHF and S-MR4-MCDHF calculations. The former optimization scheme is based on S substitutions from the MR3 set of reference configurations, i.e., $\{5s^25p6s, 5s^25p5d, 5s5p^3\}$, whereas the latter scheme also includes the $5s^25p7s$ configuration in the so-called MR4 multireference. When all four configurations are included in the MR, the $7s$ orbital is part of the spectroscopic orbitals and it is, thus, placed in parentheses in row 3, which displays the $i = 2$ correlation orbital layer. In columns 3 and 4, the numbers of generated CSFs, N_{CSFs} , are, respectively, given for each of the two different optimization schemes. Columns 5 and 6 display the number of CSFs for the subsequent RCI calculations when additional VV correlations have been accounted for by D substitutions from the valence orbitals.

i	Layers of correlation orbitals	N_{CSFs}		$N_{\text{CSFs, RCI}}$	
		MR3	MR4	MR3	MR4
	None (MR)	9	11		
1	$6p, 4f$	2097	2479	2570	3093
2	$(7s), 7p, 6d, 5f$	4349	4820	6574	7295
3	$8s, 8p, 7d, 6f, 5g$	7054	7886	13 195	14 789
4	$9s, 9p, 8d, 7f, 6g$	9759	10 952	21 904	24 689
5	$10s, 10p, 9d, 8f, 7g, 6h$	12 563	14 120	34 056	38 498
6	$11s, 11p, 10d, 9f, 8g, 7h$	15 367	17 288	49 038	55 551
7	$12s, 12p, 11d, 10f, 9g, 8h, 7i$	18 242	20 529	68 286	77 435
8	$13s, 13p, 12d, 11f, 10g, 9h, 8i$	21 117	23 770	91 108	103 403

and can be merged with important closely degenerate configurations, forming the multi-reference (MR) space. When only one configuration is considered, the latter reduces to a single-reference (SR) space. Applying the rules for coupling angular momenta, the reference configurations produce a number of CSFs that account for the major electron correlation effects or else what is known as static correlation [29]. The spectroscopic (occupied) orbitals that take part in this initial calculation are kept frozen in all following MCDHF and RCI calculations.

The initial approximation of the wave functions is improved by gradually augmenting the atomic-state expansions with CSFs that interact, i.e., have nonzero matrix elements, with the ones that are generated by the reference configurations. These CSFs are, due to the one- and two-body character of the Hamiltonian, obtained from configurations generated by allowing single (S) and, possibly, double (D) substitutions from orbitals of the configurations in the MR to an active set (AS) of correlation orbitals. The AS is systematically increased by introducing, at each step, a layer of correlation orbitals consisting of at most one orbital per angular symmetry. The correlation orbital layers in the AS are optimized in successive MCDHF calculations, in which the previously generated orbitals are kept frozen. It should, therefore, be highlighted that the correlation orbitals of the MCDHF-RCI methods differ from the virtual orbitals of the CI-DFS method in that the former orbitals are variationally optimized through the MCDHF procedure, while the latter orbitals are generated according to Eq. (2).

The CSFs can, based on the nature of the SD substitutions, be classified into CSFs that capture valence-valence (VV), core-valence (CV), and core-core (CC) electron correlation effects [[47], p.71]. The radial orbital basis is obtained by performing MCDHF calculations, where all, or some, of these classes of CSFs are taken into account. Additional electron correlation effects, captured by CSFs formed from higher-order substitutions, i.e., triple (T), quadruple (Q), etc., can be considered in the subsequent RCI calculations. In general, the selection of the CSFs that take part in the MCDHF and RCI

calculations depends on the shell structure of the atom at hand and the atomic properties under investigation.

The computations of the hyperfine factors A_{el} and B_{el} are usually challenging due to their high sensitivity to different electron correlation effects. To investigate and assess the role of the separate electron correlation contributions, three alternative MCDHF-RCI computational approaches were employed in this work. Below, we describe the three independent multiconfiguration calculations and present their individual results.

1. S-MR-MCDHF calculations

In this first computational approach, the MCDHF calculations were performed with CSF expansions that were produced by allowing S substitutions from an MR set of configurations. Due to the one-body nature of the hyperfine operators (5) and (6), the S substitutions play an important role in the calculations of hyperfine structures. This also agrees with the perturbative analysis conducted, e.g., in Ref. [48]. CSFs generated by S substitutions interact with at least one of the CSFs built from the MR configurations. By using more than one reference configuration, the current computational strategy further takes into account important D and T substitutions from the targeted $5s^25p6s$ configuration. The T substitutions are quite crucial. The latter may be decomposed into D substitutions followed by S substitutions. CSFs built from configurations that differ by T substitutions from the targeted configuration, thus, interact through the one-body hyperfine operators with the energetically important CSFs generated by D substitutions.

Two separate S-MR-MCDHF calculations were performed, using different MR spaces, which are, respectively, denoted MR3 and MR4. Aside from the $5s^25p6s$ configuration of the targeted states, the MR3 set incorporates the $5s^25p5d$ and $5s5p^3$ configurations. The $5s5p^3$ configuration was found to strongly influence the odd levels of Sn I due to its large mixing [49]. The MR4 set further includes the $5s^25p7s$ configuration accounting for the LS -term dependence [47],

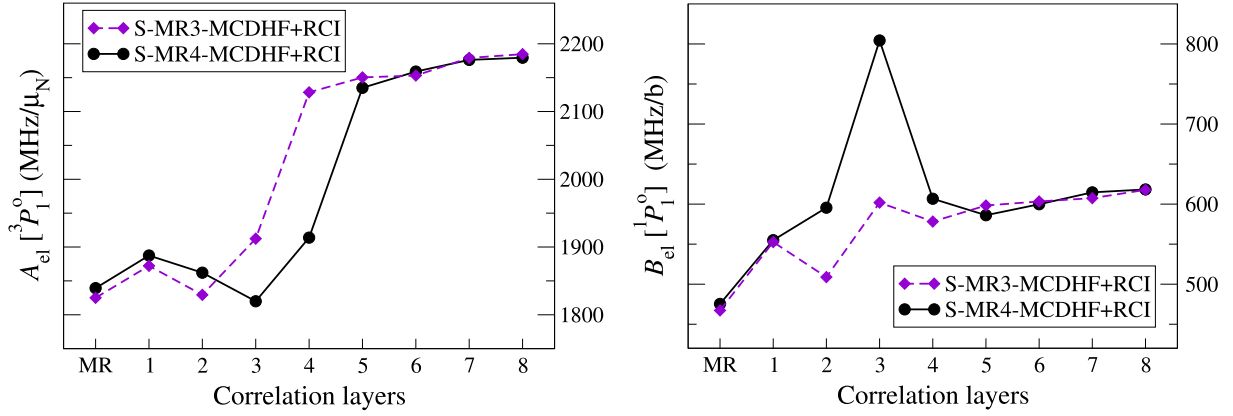


FIG. 1. The convergence patterns of the electronic hyperfine factors $A_{el}[^3P_1^0]$ (in MHz/ μ_N) and $B_{el}[^1P_1^0]$ (in MHz/b) as functions of the correlation orbital layers. The radial orbital basis was obtained by applying two different optimization schemes with respect to the selected MR spaces. The purple dashed lines connect the values resulting from the S-MR3-MCDHF optimization, where three reference configurations are included in the MR, and the black solid lines link the resulting values from the S-MR4-MCDHF optimization, where the MR was extended to include four reference configurations. Both sets of values are the results from the RCI calculations that followed the orbital optimization step. For further details, see text in Sec. III A 1.

i.e., the difference between the $6s$ orbital of the $5s^25p6s\ ^3P_1^0$ and $5s^25p6s\ ^1P_1^0$ states. The calculations are performed in the EOL scheme for the average of the configuration states included in the MR.

In both S-MR-MCDHF calculations, all spectroscopic orbitals were opened for S substitutions. The layers of correlation orbitals that were progressively added to the AS are shown in column 2 of Table I. In total, eight correlation orbital layers were built, corresponding to the $13s13p12d11f10g9h8i$ set of orbitals. For every additional correlation orbital layer i , the resulting numbers of CSFs, N_{CSFs} , in the MR3 and MR4 optimization schemes are, respectively, given in columns 3 and 4 of Table I. As seen in Table I, the configurations in each of the MR3 and MR4 sets generate 9 and 11 CSFs.

The RCI calculations included CSFs that were produced by allowing D substitutions from the valence orbitals of the configurations in the MR. In this manner, VV electron correlation effects were ultimately captured. D substitutions from core orbitals were not considered to keep the number of CSFs at a manageable level. The numbers of CSFs for the RCI calculations are given in columns 5 and 6 of Table I.

The resulting values of the hyperfine electronic factors $A_{el}[^3P_1^0]$ and $B_{el}[^1P_1^0]$ from applying the two different optimization schemes are shown in Fig. 1 with the labels S-MR3-MCDHF+RCI and S-MR4-MCDHF+RCI, respectively. As seen in Fig. 1, both computed electronic factors are effectively converged. For the largest CSF expansions, the variations between the S-MR3-MCDHF+RCI and S-MR4-MCDHF+RCI results are insignificant. As the final results of this first MCDHF-RCI computational approach, we take the resulting values from the largest S-MR4-MCDHF+RCI calculation, corresponding to expansions with 103 403 CSFs, so that

$$A_{el}[^3P_1^0] = 2180 \text{ MHz}/\mu_N; \quad B_{el}[^1P_1^0] = 622 \text{ MHz/b.} \quad (12)$$

2. SrD-SR-MCDHF calculations

In the second computational approach, the MCDHF calculations were performed in the EOL scheme for the average of the $5s^25p6s\ ^1,3P_1^0$ states using CSF expansions that were produced by S and restricted double (rD) substitutions from the SR configuration of the targeted states, i.e., $5s^25p6s$.

More specifically, S substitutions from all spectroscopic orbitals and D substitutions, restricted by the limitation of leaving maximum one hole in core orbitals with $n < 5$, were enabled. In this manner, the generated CSFs in the orbital optimization phase also captured CV correlation effects. The AS was systematically increased to include layers with one additional correlation orbital of the s , p , d , f , and g angular symmetries, respectively, apart from the very last, eighth, layer, which only contained the s , p , d , and f symmetries. The largest multiconfiguration expansions were then built on the $14s13p12d11f11g$ set of orbitals. For every layer of correlation orbitals that was added in the SrD orbital optimization phase, the resulting values of the electronic factors $A_{el}[^3P_1^0]$ and $B_{el}[^1P_1^0]$ are shown in Fig. 2 (magenta circles). We note that, after adding the sixth layer of correlation orbitals, both the $A_{el}[^3P_1^0]$ and $B_{el}[^1P_1^0]$ values were converged. For this reason, the CSFs produced during this first phase by allowing SrD substitutions to the seventh and eighth layers were not considered in the subsequent RCI calculations.

The RCI calculations were performed in two phases, which, respectively, allowed SD and SDT substitutions. In the so-called SD and SDT phases, the multiconfiguration expansions were obtained by systematically increasing the AS, the maximum angular momentum quantum number l within the AS, and the number of opened spectroscopic orbital shells. The computed electronic factors $A_{el}[^3P_1^0]$ and $B_{el}[^1P_1^0]$ for the different multiconfiguration expansions that were used in the SD and SDT phases are given in Table II. The $A_{el}[^3P_1^0]$ and $B_{el}[^1P_1^0]$ values are also plotted in Fig. 2 for both SD (green squares) and SDT (blue triangles) approaches. The numbers 10–26 on the x axis of Fig. 2 are equivalent to the labels

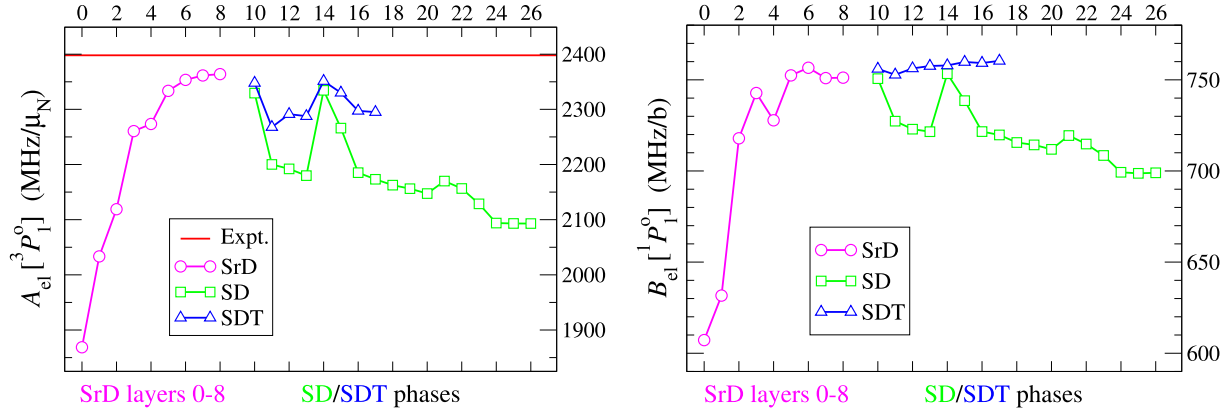


FIG. 2. The electronic hyperfine factors $A_{\text{el}}[{}^3P_1^0]$ (in MHz/ μ_N) and $B_{\text{el}}[{}^1P_1^0]$ (in MHz/b) based on three computational approaches: the SrD (magenta circles), SD (green squares), and SDT (blue triangles). On the x axes, the number 0 indicates the DHF computation, the numbers 1–8 represent the consecutive layers of correlation orbitals developed in the SrD phase of the calculations, and the numbers 10–26 match the labels of the multiconfiguration expansions presented in column 1 of Table II, corresponding to the calculations performed in the SD and SDT phases. The red straight horizontal line on the left graph represents the experimental value $A_{\text{el}}^{\text{expt}}[{}^3P_1^0] = 2398$ MHz/ μ_N from Ref. [12]. See also text in Sec. III A 2.

displayed in column 1 of Table II. For each calculation, column 2 of Table II provides the principal quantum number n of the deepest orbital shell that was opened for substitutions, e.g., $n \geq 4$ involves substitutions from $4s$, $4p$, $4d$, $5s$, $5p$, $6s$, and column 3 displays the AS of orbitals to which the substitutions were allowed. As a reference, the $A_{\text{el}}[{}^3P_1^0]$ and $B_{\text{el}}[{}^1P_1^0]$ values resulting from the sixth layer of the SrD phase are

presented in the second row of Table II, while the first row displays the electronic factors from the DHF computation, restricted to two CSFs.

After generating CSF expansions by allowing substitutions from the $n \geq 3$ spectroscopic shells to the $12s11p10d9f10g$ set of orbitals in the label 24 calculation, the electronic factors computed in the SD phase were ultimately converged.

TABLE II. The computed electronic factors $A_{\text{el}}[{}^3P_1^0]$ (in MHz/ μ_N) and $B_{\text{el}}[{}^1P_1^0]$ (in MHz/b) for various multiconfiguration expansions that were used in the RCI phases following the SrD-SR-MCDHF calculations. In each RCI phase, the considered CSFs were, respectively, generated based on SD (columns 4 and 6) and SDT (columns 5 and 7) substitutions from the opened spectroscopic shells displayed in column 2 to the AS of correlation orbitals given in column 3. The first row contains the resulting $A_{\text{el}}[{}^3P_1^0]$ and $B_{\text{el}}[{}^1P_1^0]$ values from the DHF computation, where only the CSFs of the two targeted states were considered, and the second row displays the converged results from the SrD orbital optimization phase after the sixth correlation orbital layer was added. The labels given in column 1 correspond to the labels used on the horizontal axes of Fig. 2.

Label	Open shells	Active orbital set	$A_{\text{el}}[{}^3P_1^0]$ (MHz/ μ_N)		$B_{\text{el}}[{}^1P_1^0]$ (MHz/b)	
			SD	SDT	SD	SDT
0	Phase 1: DHF computation			1869		607
6	Phase 1: SrD correlation layer 6			2353		757
10	$n \geq 5$	$8s7p$	2329	2348	751	756
11	$n \geq 4$	$7s6p5d4f$	2200	2268	727	753
12	$n \geq 4$	$8s7p5d4f$	2192	2291	723	756
13	$n \geq 4$	$8s7p5d4f5g$	2180	2288	722	758
14	$n \geq 4$	$9s8p$	2335	2351	753	758
15	$n \geq 4$	$9s8p5d$	2266	2330	739	760
16	$n \geq 4$	$9s8p5d4f$	2185	2297	722	759
17	$n \geq 4$	$9s8p5d4f5g$	2173	2295	720	760
18	$n \geq 4$	$10s9p6d5f6g$	2163		716	
19	$n \geq 4$	$11s10p7d6f7g$	2156		714	
20	$n \geq 4$	$12s11p10d9f10g$	2147		712	
21	$n \geq 3$	$9s8p5d4f5g$	2170		719	
22	$n \geq 3$	$10s9p6d5f6g$	2157		715	
23	$n \geq 3$	$11s10p7d6f7g$	2129		709	
24	$n \geq 3$	$12s11p10d9f10g$	2094		699	
25	$n \geq 3$	$13s12p11d10f11g$	2093		699	
26	$n \geq 2$	$12s11p10d9f10g$	2089		698	
	Expt. [12]			2398(2)		

Extending further the multiconfiguration expansions by either adding one more layer of correlation orbitals (label 25 calculation) or opening the $n = 2$ spectroscopic shells (label 26 calculation) has nearly no effect on the $A_{\text{el}}[{}^3P_1^0]$ and $B_{\text{el}}[{}^1P_1^0]$ values (see columns 4 and 6 in Table II). The multiconfiguration expansions used in the label 24 calculation of the SD phase constituted the starting point for the RCI calculations of the SDT phase, which followed a pattern similar to the SD approach for generating the CSFs. Yet, the number of CSFs produced by T substitutions grew very rapidly, and the limits of the computational resources available to us were reached after performing the label 17 calculation. It should be pointed out that the latter calculation included 4406086 CSFs and took 37 days of wall time on the computer cluster at our disposal (6×96 CPU @ 2.4 GHz with 6×256 GB RAM). For the next calculation, the label 18 calculation, 17817617 CSFs were generated, which exceeded the capacity of the cluster. The $A_{\text{el}}[{}^3P_1^0]$ and $B_{\text{el}}[{}^1P_1^0]$ values computed in the SDT phase were, thus, not fully converged.

The dependence of the resulting $A_{\text{el}}[{}^3P_1^0]$ and $B_{\text{el}}[{}^1P_1^0]$ values on CSF expansions formed from different classes of electron substitutions is well illustrated in Fig. 2. We notice that, in the SD phase, the values of the computed hyperfine factors decrease compared to the SrD results. On the other hand, when T substitutions are also considered, the values of the computed properties increase in relation to the respective calculations of the SD phase. This behavior has also been observed in many earlier calculations of hyperfine structures [35,50–55]. When performing RCI calculations by allowing D substitutions from core orbitals, CSFs that account for CC correlation effects are included in the atomic-state expansions. These CSFs have relatively large mixing coefficients due to their important contribution to the total energy and, as a result, the mixing coefficients of CSFs describing effects, such as spin and orbital polarization, that are more important for hyperfine interactions take lower values. This is eventually counterbalanced by the inclusion of CSFs generated from T substitutions.

Further, the comparison between the two graphs in Fig. 2 illustrates the similar synchronous dependence of the computed $A_{\text{el}}[{}^3P_1^0]$ and $B_{\text{el}}[{}^1P_1^0]$ values on the increasing multiconfiguration expansions in the SrD (magenta circles) and SD (green squares) phases of the computations. This correlated behavior between computed A_{el} and B_{el} hyperfine interaction factors has also been observed in numerous previous works [13,56–59]. The M1 and E2 hyperfine factors are obtained by evaluating the expectation values of the operators (5) and (6), respectively. These expectation values are expressed in terms of reduced matrix elements of the operators above, involving radial integrals that have a common dependence on the radial factor r^{-3} . Although it is not directly obvious from Eqs. (5) and (6), the common r^{-3} dependence is explained by the different structures of the relevant one-electron matrix elements in the nonrelativistic limit [[60], Sec. 5.2]. For this reason, when, at each step of the computations, the same CSF expansions are considered, the values of the $A_{\text{el}}[{}^3P_1^0]$ and $B_{\text{el}}[{}^1P_1^0]$ factors will most likely synchronously oscillate (see also, e.g., the curves a_{dip} and b_{quad} in Fig. 8 of Ref. [48]).

In consideration of the foregoing, the relative shifts in the $A_{\text{el}}[{}^3P_1^0]$ and $B_{\text{el}}[{}^1P_1^0]$ values induced by an additional MCDHF, or RCI, calculation are expected to be proportional, i.e.,

$$\Delta A_{\text{el}}/A_{\text{el}} \approx \Delta B_{\text{el}}/B_{\text{el}}. \quad (13)$$

The equation above may be transformed into a relation in which the computed $A_{\text{el}}[{}^3P_1^0]$ and $B_{\text{el}}[{}^1P_1^0]$ values are related to the corresponding experimental $A_{\text{el}}^{\text{expt}}[{}^3P_1^0]$ and $B_{\text{el}}^{\text{expt}}[{}^1P_1^0]$ values according to

$$|A_{\text{el}} - A_{\text{el}}^{\text{expt}}|/A_{\text{el}}^{\text{expt}} \approx |B_{\text{el}} - B_{\text{el}}^{\text{expt}}|/B_{\text{el}}^{\text{expt}}. \quad (14)$$

The latter equation can then be used to adjust the computed $B_{\text{el}}[{}^1P_1^0]$ factor by applying a semiempirical shift based on the known error in the computed $A_{\text{el}}[{}^3P_1^0]$ factor. Given the experimental result $A_{\text{el}}^{\text{expt}}[{}^3P_1^0] = 2398$ MHz/ μ_N from Ref. [12], Eq. (14) was used to adjust the resulting $B_{\text{el}}[{}^1P_1^0]$ values from all three phases of the calculations, i.e., SrD, SD, and SDT. This leads to the following “shifted” values: $B_{\text{el}}(\text{SrD})^{\text{shifted}} = 759$ MHz/b, $B_{\text{el}}(\text{SD})^{\text{shifted}} = 800$ MHz/b, and $B_{\text{el}}(\text{SDT})^{\text{shifted}} = 793$ MHz/b.

Looking at Fig. 2 and Table II, one notices that the $B_{\text{el}}[{}^1P_1^0]$ value (in contrast to the $A_{\text{el}}[{}^3P_1^0]$ value) is overall insensitive to T substitutions. That being so, the result from the largest completed calculation in the SDT phase, i.e., $B_{\text{el}}[{}^1P_1^0] \equiv B_{\text{el}}(\text{SDT}) = 760$ MHz/b, is considered reliable and taken into account in the evaluation of the final $B_{\text{el}}[{}^1P_1^0]$ result for the current SrD-SR-MCDHF+RCI approach. By taking the average of the above-mentioned four values, we ultimately arrive at

$$B_{\text{el}}[{}^1P_1^0] = 778 \text{ MHz/b}. \quad (15)$$

3. SrD-MR-MCDHF calculations

In the third computational approach, the MCDHF calculations were performed in the EOL scheme for the average of the $5s^25p6s$ ${}^1,3P_1^0$ states using CSF expansions produced by allowing SrD substitutions from a set of MR configurations and are, therefore, denoted SrD-MR-MCDHF. By allowing S and D substitutions from the MR space, important T and Q substitutions from the targeted $5s^25p6s$ configuration were also taken into account. To determine the MR space, a preliminary SD-SR-MCDHF calculation was carried out, using CSFs that were formed by enabling SD substitutions from the valence orbitals ($n \geq 5$) to a first layer of correlation orbitals, i.e., $7s$, $6p$, $6d$, and $4f$. After analyzing the LS composition of the two targeted states (see Table III), we defined an MR composed of the $5s^25p6s$, $5p^36s$, and $5s5p5d6s$ configurations. The MR was restricted to the three leading configurations due to the limitations of our computational resources. This strategy for defining the reference configurations differs from the one used in Sec. III A 1, thus leading to different MR sets.

In the SrD-MR-MCDHF calculations, the $4d$, $5s$, $5p$, $5d$, and $6s$ spectroscopic orbitals were opened for SD substitutions, with the restriction that there was at most one substitution from the $4d$ core orbital. All other inner-core subshells were kept closed. The polarization of the $4d$ orbital was, thereby, taken into account together with VV correlation effects. The AS was systematically increased to include layers

TABLE III. The LS composition of the two targeted $5s^25p6s\ ^1\ ^3P_1^o$ states after performing an initial SD-SR-MCDHF calculation. The percentages of the four most dominant LS components are solely displayed. The first percentage value corresponds to the assigned configuration and term.

Pos.	Conf.	LSJ	LS composition
1	$5s^25p6s$	$^3P_1^o$	$0.761 + 0.186\ 5s^25p6s\ ^1P^o + 0.016\ 5p^36s\ ^3P^o + 0.010\ 5s5p5d6s\ ^3P^o$
2	$5s^25p6s$	$^1P_1^o$	$0.761 + 0.185\ 5s^25p6s\ ^3P^o + 0.017\ 5p^36s\ ^1P^o + 0.009\ 5s5p5d6s\ ^1P^o$

with one additional correlation orbital of the s , p , d , and f symmetries. The effects of orbitals with higher angular symmetries on the computation of hyperfine structures are generally known to be small, justifying the choice of the “ f limit” [61]. Overall, nine correlation orbital layers were built, corresponding to the $15s14p14d12f$ set of orbitals.

Table IV displays the computed excitation energies $E[^3P_1^o]$ and $E[^1P_1^o]$, energy separations $\Delta E = E[^1P_1^o] - E[^3P_1^o]$, hyperfine electronic factors $A_{el}[^3P_1^o]$ and $B_{el}[^1P_1^o]$, and numbers of CSFs, N_{CSFs} , as functions of the increasing AS of correlation orbitals. The values associated with the initial MR calculation that corresponds to 17 CSFs are given in the first row of Table IV. After optimizing nine layers of correlation orbitals, all computed properties were effectively converged. One should note that the number of CSFs in the expansions of the final SrD-MR-MCDHF calculation exceeded one million. At this point, the predicted energy separation agrees with the observed value to within 3%, which provides an initial assessment of the computed hyperfine factors. The convergence patterns of the computed $A_{el}[^3P_1^o]$ and $B_{el}[^1P_1^o]$ values with respect to the increasing number of correlation orbital layers optimized in the SrD-MR-MCDHF calculations are also graphically illustrated in Fig. 3.

As a final step, an RCI calculation was carried out using the $15s14p14d12f$ orbital set. For this RCI calculation, the CSFs were produced by enabling S substitutions from all spectroscopic orbitals, along with D substitutions from the

$4p$, $4d$, $5s$, $5p$, $5d$, and $6s$ orbitals, with the two following restrictions: (1) at most one substitution from the $4p$ orbital and (2) no simultaneous substitutions from the $4p$ and $4d$ orbitals. Hence, CC correlation effects were solely captured by the allowed D substitutions from the $4d$ orbital. Based on preliminary RCI calculations that used a smaller orbital basis, the polarization effect of the $4s$ core orbital was deduced to be significant too. However, the capacity of the computer cluster at our disposal did not allow us to include it. The SrD-MR-MCDHF+RCI results are presented in the second last row of Table IV and correspond to atomic-state expansions with 3 583 001 CSFs.

At each step of the calculations that followed this third MCDHF-RCI computational approach, the atomic-state expansions were restricted to CSFs that interact with the ones generated by the MR configurations. Indicatively, we mention that the number of CSFs in the atomic-state expansions of the final RCI calculation, initially, were 5 313 860. It has been shown, in previous works, that such reduction of CSFs does not bring any major losses in accuracy [64–66]. In any case, the effect of limiting the number of CSFs to the “interacting” ones was also evaluated in this work. It was deduced that utilizing the full CSF space causes the $A_{el}[^3P_1^o]$ and $B_{el}[^1P_1^o]$ values to rise by ~ 7 MHz/ μ_N and ~ 1 MHz/b, respectively. In addition, it was estimated that when orbitals of the g and h angular symmetries are added to the orbital basis, the $A_{el}[^3P_1^o]$ value further increases by ~ 3 MHz/ μ_N , while the change in

TABLE IV. The convergence of the energies and hyperfine factors A_{el} (in MHz/ μ_N) and B_{el} (in MHz/b) for the $^1\ ^3P_1^o$ states as the MR orbital basis extends to include nine layers of correlation orbitals optimized in the SrD-MR-MCDHF calculations. The results after the subsequent RCI calculations are also presented in the second last row. The computed excitation energies of the $^3P_1^o$ and $^1P_1^o$ states are, respectively, presented (in cm^{-1}) in columns 2 and 3, whereas the evaluated energy separations are displayed in column 4. For comparison, the observed energies are shown in the last row. In each of the columns 5 and 6, the values of the $A_{el}[^3P_1^o]$ and $B_{el}[^1P_1^o]$ factors are given. The last column exhibits the numbers of generated CSFs for every additional correlation orbital layer.

Correlation layer	Energies (cm^{-1})			$A_{el}[^3P_1^o]$	$B_{el}[^1P_1^o]$	N_{CSFs}
	$^3P_1^o$	$^1P_1^o$	$^1P_1^o - ^3P_1^o$			
None (MR)	33 301	38 002	4701	1869	613	17
1	34 327	38 990	4663	2044	586	16 593
2	34 789	39 323	4534	2055	586	57 086
3	34 644	39 154	4510	2092	587	122 610
4	34 587	39 072	4485	2109	591	212 946
5	34 544	39 020	4476	2120	596	328 094
6	34 529	39 004	4475	2117	590	468 054
7	34 521	38 993	4472	2121	593	632 826
8	34 519	38 987	4468	2119	590	822 410
9	34 517	38 984	4467	2120	592	1 036 806
+ RCI	34 374	38 938	4565	2169	716	3 583 001
Expt. [62,63]	34 914	39 257	4343			

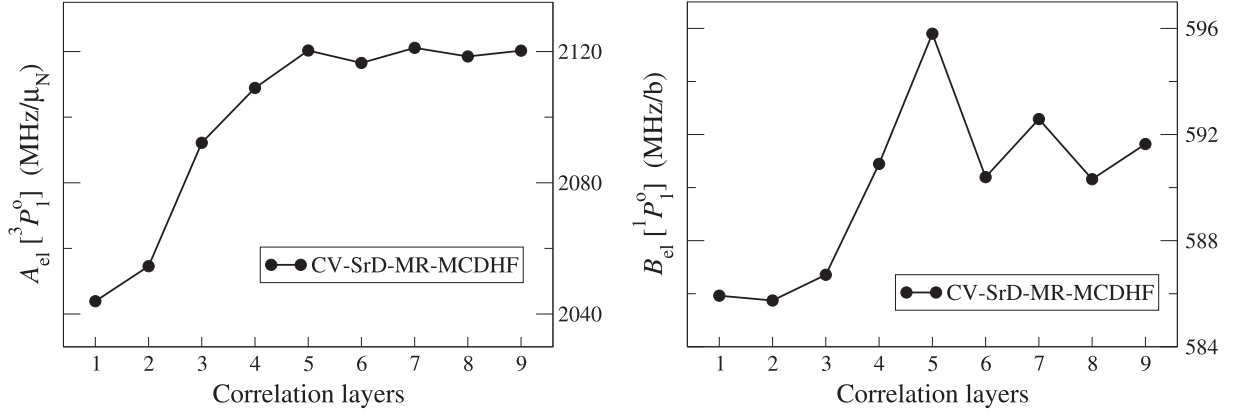


FIG. 3. The convergence patterns of the electronic hyperfine factors $A_{el}[^3P_1^0]$ (in MHz/ μ_N) and $B_{el}[^3P_1^0]$ (in MHz/b) with the increasing number of correlation orbital layers optimized in the SrD-MR-MCDHF calculations. For the computational details, see text in Sec. III A 3.

the $B_{el}[^1P_1^0]$ value is negligible. Considering the above corrections to the final SrD-MR-MCDHF+RCI results, we finally arrive at

$$A_{el}[^3P_1^0] = 2179 \text{ MHz}/\mu_N; \quad B_{el}[^1P_1^0] = 717 \text{ MHz/b}. \quad (16)$$

4. Sensitivity to orbital bases and CSF expansions

As previously seen, different calculations based on the same general method, i.e., the MCDHF-RCI, and performed with the same program, the GRASP2018 computer package, lead to different results. The $A_{el}[^3P_1^0]$ and $B_{el}[^1P_1^0]$ values obtained with the three approaches do agree within approximately 10%. The differences in the S-MR-MCDHF, SrD-SR-MCDHF, and SrD-MR-MCDHF approaches lie in the choice of their respective orbital bases and CSF expansions, each with its benefits and drawbacks. In this subsection, we investigate the sensitivity of the SrD-SR-MCDHF and SrD-MR-MCDHF approaches by arbitrarily interchanging their orbital bases and CSF expansions. In addition to the $A_{el}[^3P_1^0]$ and $B_{el}[^1P_1^0]$ values, we also discuss the $A_{el}[^1P_1^0]/A_{el}[^3P_1^0]$ and $B_{el}[^3P_1^0]/B_{el}[^1P_1^0]$ ratios, as it was recently done with the experimental results presented in Ref. [12], to provide additional information about the sensitivity of our calculations.

For each of the two above-mentioned methods, the final results were obtained by performing RCI computations. These results are shown in the first two rows of Table V using

the labels SrD-MR/SrD-MR and SrD-SR/SrD-SR, for the SrD-MR-MCDHF and SrD-SR-MCDHF approaches, respectively (the notation X/Y defines the orbital basis from X and CSF expansion from Y). Two additional sets of computations were performed: one combining the SrD-SR-MCDHF orbital basis and the SrD-MR-MCDHF CSF space (see SrD-SR/SrD-MR in Table V) and one combining the SrD-MR-MCDHF orbital basis and the SrD-SR-MCDHF CSF space (see SrD-MR/SrD-SR in Table V). Minor changes in the CSF spaces were required. The SR active space was restricted to the s , p , d , and f symmetries as the MR orbital basis is limited to $l_{\max} = 3$, and the SrD-MR-MCDHF CSF space was limited to only six correlation layers.

Although far from being in perfect agreement, the results presented in Table V are consistent. The effect of replacing the orbital set, for a given CSF expansion, is surprisingly small. Additionally, the $A_{el}[^1P_1^0]/A_{el}[^3P_1^0]$ and $B_{el}[^3P_1^0]/B_{el}[^1P_1^0]$ values are also presented in Table V, where it is seen that the former ratio is less stable than the latter. The computed $A_{el}[^1P_1^0]/A_{el}[^3P_1^0]$ values vary from 0.124 to 0.185, which corresponds to a deviation of 50% from the lowest value. By considering a simple term mixing between the $^3P_1^0$ and $^1P_1^0$ terms, it is shown in the Appendix that this sensitivity is expected. Using the same model, one further explains the steadier values of the $B_{el}[^3P_1^0]/B_{el}[^1P_1^0]$ ratio. The computed $B_{el}[^3P_1^0]/B_{el}[^1P_1^0]$ values range from -0.240 to -0.270 , which is in very good agreement with the experimental value of

TABLE V. The electronic hyperfine factors $A_{el}[^3P_1^0]$ (in MHz/ μ_N) and $B_{el}[^1P_1^0]$ (in MHz/ μ_N) as well as the $A_{el}[^1P_1^0]/A_{el}[^3P_1^0]$ and $B_{el}[^3P_1^0]/B_{el}[^1P_1^0]$ ratios, computed for six different combinations of orbital basis sets and CSF spaces. The SrD-SR-MCDHF and SrD-MR-MCDHF computational approaches are compared by expanding the total wave function over the largest CSF expansion of the one method and using the orbital basis of the other method. Adjustments were made in the CSF expansions due to the specific properties of the orbital bases obtained in the two different approaches. For details, see text in Sec. III A 4.

Orb. basis	CSF expansions	$A_{el}[^3P_1^0]$	$A_{el}[^1P_1^0]/A_{el}[^3P_1^0]$	$B_{el}[^1P_1^0]$	$B_{el}[^3P_1^0]/B_{el}[^1P_1^0]$
SrD-MR	SrD-MR	2179	0.185	717	-0.240
SrD-SR	SrD-SR	2295	0.124	760	-0.250
SrD-MR	SrD-SR (<i>spdf</i> limit)	2303	0.126	739	-0.254
SrD-SR	SrD-SR (<i>spdf</i> limit)	2297	0.126	722	-0.263
SrD-MR	SrD-MR (6 layers)	2161	0.183	709	-0.243
SrD-SR	SrD-MR (6 layers)	2168	0.158	718	-0.270

TABLE VI. The numbers of CSFs and the resulting energy separations between the targeted ${}^3P_1^0$ and ${}^1P_1^0$ states for each virtual orbital layer used in the CI-DFS calculations. Two approaches, the direct (full basis) and the one based on perturbation theory (PT), were implemented. The numbers of additional determinants ND_{PT} , built using PT, are displayed in parentheses. $\Delta E = E[{}^1P_1^0] - E[{}^3P_1^0]$ are the energy separations in cm^{-1} . The numbers of virtual orbital layers given in column 1 correspond to the labels used on the horizontal axes of Fig. 4, and column 2 displays the respective orbital basis sets. For details see Sec. III B.

Virtual layer	Orbital basis set	Full basis		Perturbation theory		
		N_{CSFs}	ΔE (cm^{-1})	ND_{PT}	N_{CSFs}	ΔE (cm^{-1})
1	$6s5p4d$	1 520	4 537	(1184)	886	4 538
2	$6s5p5d4f$	39 021	4 868	(69 759)	23 504	4 868
3	$7s6p5d4f$	80 018	4 930	(123 905)	47 828	4 930
4	$7s6p6d5f$	198 543	4 880	(341 769)	119 338	4 880
5	$8s7p6d5f$	282 859	4 888	(452 698)	169 363	5 102
6	$8s7p7d6f$	482 408	4 859	(819 851)	289 765	5 069
7	$9s8p7d6f$	610 043	4 858	(987 563)	365 491	5 279
8	$9s8p8d7f$	890 616	4 842	(2 343 509)	534 785	5 268
9	$10s9p8d7f$	1 061 570	4 848	(2 942 992)	636 212	5 495
10	$10s9p9d8f$			(4 691 292)	854 398	5 508
Expt. [62,63]			4 343			4 343

–0.25(2) [12]. On the other hand, the $A_{\text{el}}[{}^1P_1^0]/A_{\text{el}}[{}^3P_1^0]$ values (ranging from 0.124 to 0.185) do not agree with the experimental result of 0.0517(2) [12].

B. CI-DFS calculations

In this last set of calculations, which is based on the CI-DFS theory, we used for all Sturmian functions the same reference energy, namely, the one of the hydrogenic $5s$ state. Allowing SD substitutions from all spectroscopic orbitals with $n \leq 5$, together with the $6s$ and $6p$ orbitals, to an increasing AS of virtual orbitals results in a large number of configurations and huge matrices for the numerical diagonalization. By freezing the $1s$, $2s$, and $2p$ orbitals and by using perturbation theory (PT) to build low-lying closed shells and highly excited states, we were able to extend the one-electron basis to the $12s11p10d9f$ set of orbitals. For the three smallest orbital basis sets, T substitutions from the $n = 4, 5$ orbitals, in addition to the $6s$ and $6p$ orbitals, were included, although their influence was smaller than the uncertainty level we aim at.

In the CI-DFS calculations of the hyperfine electronic factors A_{el} , the nuclear dipole moment distribution, or else Bohr-Weisskopf (BW) effect, was also taken into account. This was done by multiplying the operator $\mathbf{T}^{(1)}$ in Eq. (7) by a nuclear distribution function $F_{\text{BW}}(r)$. In the homogeneous-nuclear-current-distribution approximation, this function is determined by the nuclear radius R_N so that [67]

$$F_{\text{BW}}(r) = \begin{cases} (r/R_N)^3, & r \leq R_N \\ 1, & r > R_N. \end{cases} \quad (17)$$

The calculated BW correction was $\lesssim 0.001\%$ and $\lesssim 0.1\%$, for the ${}^3P_1^0$ and ${}^1P_1^0$ states, respectively. Analogously, a nuclear quadrupole moment distribution function can be introduced for the B_{el} property as a factor to the operator $\mathbf{T}^{(2)}$ in Eq. (8). For the shell model, i.e., assuming that the quadrupole distribution is concentrated around the nuclear radius, this function

is given by [67]

$$F_Q(r) = \begin{cases} (r/R_N)^5, & r \leq R_N \\ 1, & r > R_N. \end{cases} \quad (18)$$

The latter effect is on the level of 0.1% for both considered states, which is in good agreement with the estimations made for the Cd ground state in [68].

For each virtual orbital layer that was used in the CI-DFS calculations, the corresponding orbital basis set, numbers of CSFs, and computed energy separations ΔE between the targeted ${}^3P_1^0$ and ${}^1P_1^0$ states are listed in Table VI. One can see that the resulting energy difference $\Delta E = E[{}^1P_1^0] - E[{}^3P_1^0]$ from the direct (full basis) calculations is well converged, in contrast to the PT calculations, where the ΔE value is not saturated. In Fig. 4, the convergence patterns of the computed $A_{\text{el}}[{}^3P_1^0]$ and $B_{\text{el}}[{}^1P_1^0]$ values are shown for both non-PT (solid circles) and PT (empty circles) bases. It is seen in the figure that the E2 hyperfine electronic factor $B_{\text{el}}[{}^1P_1^0]$ is more sensitive to variations of the orbital basis set, in comparison to the M1 electronic factor $A_{\text{el}}[{}^3P_1^0]$ and, for that reason, its theoretical uncertainty is larger. In addition, we observe that the results from the non-PT and PT calculations progressively diverge as the number of virtual PT orbitals increases. That being so, and taking also into account the weaker stability of the PT energy separation value, the results from the perturbative treatment can only be used for estimating the theoretical error bars (see Sec. IV A), and not for extending the basis further. The final results of the CI-DFS calculations based on the largest non-PT orbital basis set, which corresponds to 1 061 570 CSFs, are

$$A_{\text{el}}[{}^3P_1^0] = 2082 \text{ MHz}/\mu_N; \quad B_{\text{el}}[{}^1P_1^0] = 693 \text{ MHz/b.} \quad (19)$$

IV. FINAL VALUE AND EVALUATION OF ACCURACY

In Secs. III A 1–III B, four different computational approaches for evaluating the electronic hyperfine factors A_{el}

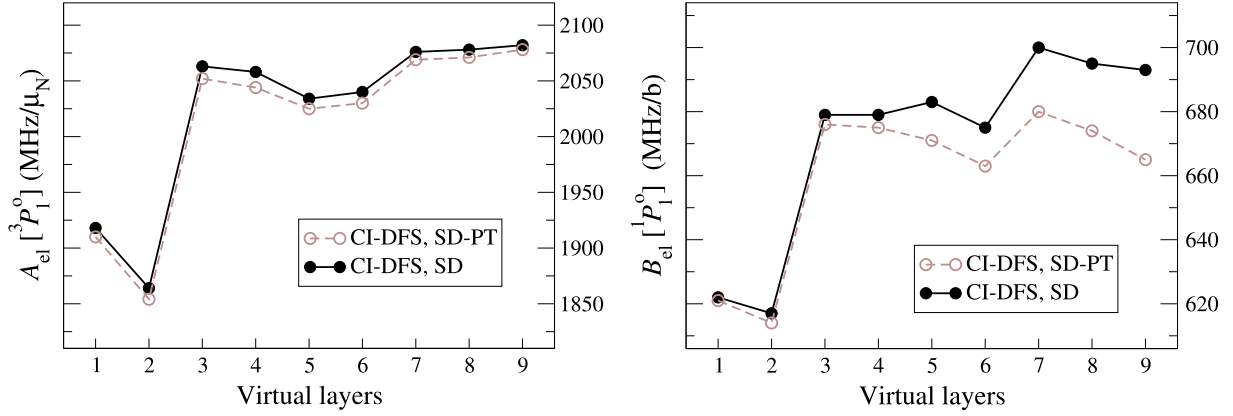


FIG. 4. The convergence of the electronic hyperfine factors $A_{el}[^3P_1^0]$ (in MHz/ μ_N) and $B_{el}[^1P_1^0]$ (in MHz/b) with the increasing number of virtual orbital layers, optimized by employing the CI-DFS method. The solid black circles represent the results from the direct (full basis) calculations, while the empty brown circles illustrate the values obtained using perturbation theory (PT). The numbers of virtual orbital layers on the x axes are equivalent to the numbers given in column 1 of Table VI. See also text in Sec. III B.

and B_{el} of the $1,^3P_1^0$ excited states in neutral tin were presented. In this section, we solely focus on $B_{el}[^1P_1^0]$ that can be used to extract the quadrupole moments Q of tin isotopes for which spectroscopic data are available. The $B_{el}[^1P_1^0]$ values obtained from the four independent sets of calculations are summarized in Table VII. By taking their average, we ultimately arrive at $B_{el}[^1P_1^0] = 703$ MHz/b.

As a crude estimate of the uncertainty of the concluding $B_{el}[^1P_1^0]$ value, we can consider the half-range of the aforementioned individual results, i.e., 78 MHz/b. Yet, if one wants to be in a position to discuss atomic, or nuclear, properties and their underlying physics, a rigorous assessment of the uncertainties of the computed values is required. In recent years, atomic physicists have been putting great efforts into providing reliable uncertainties on their theoretical results [6,35,69–71]. In line with these efforts, the following subsections take into account a number of considerations to determine the accuracy of the final $B_{el}[^1P_1^0]$ value. Some of these considerations are only applicable to one (or more) particular set(s) of calculations (see Sec. IV A), while others are analogously applied to all four separate results (see Sec. IV B). Statistical principles are implemented (see Sec. IV C), and former outcomes from computations of electronic hyperfine factors, regarding atomic states with electronic structure similar to the structure of the $5s^25p6s$ $1,^3P_1^0$ states in Sn I, are also used as an estimate of the accuracy of the $B_{el}[^1P_1^0]$ value deduced in this work (see Sec. IV D).

TABLE VII. The resulting $B_{el}[^1P_1^0]$ values (in MHz/b) from the four independent sets of calculations presented in Secs. III A 1–III B. The last row displays their average.

Methods	$B_{el}[^1P_1^0]$ (MHz/b)
S-MR-MCDHF+RCI	622
SrD-SR-MCDHF+RCI	778
SrD-MR-MCDHF+RCI	717
CI-DFS	693
Average	703

A. Model-specific uncertainties

In each of the four independent approaches that were discussed in the previous sections, the wave functions (radial orbitals and configuration-mixing coefficients) that describe the atomic states were obtained based on various approximations with respect to the orbital basis and the list of configuration states. In Sec. III A 4, the sensitivity of the SrD-SR-MCDHF+RCI and SrD-MR-MCDHF+RCI results to the orbital basis was investigated by combining the radial orbital basis obtained in one of these two computational approaches with the CSF expansions used in the RCI computations of the other approach. As seen in Table V, these combinations gave rise to $B_{el}[^1P_1^0]$ values that range from 709 MHz to 760 MHz/b. The half-range of these values yields an uncertainty of 26 Hz/b. Further, in the CI-DFS calculations, the electronic hyperfine factors were computed using both non-PT and PT orbital bases. The comparison between the non-PT and PT results for different orbital basis sets suggests an uncertainty of 70 MHz/b in the deduced $B_{el}[^1P_1^0]$. Lastly, in the instance of the SrD-SR-MCDHF calculations, the outcome for the $B_{el}[^1P_1^0]$ value is the average of four separate values. One can, thus, assume an error bar corresponding to the half-range of these values, i.e., 20 MHz/b.

B. Difference between the theoretical $A_{el}[^3P_1^0]$ and experimental $A_{el}^{exp}[^3P_1^0]$ values

The deviation of the calculated M1 hyperfine constant from the experimental value $|A_{theor} - A_{expt}|$ is often assumed to be a measure of the overall accuracy of the hyperfine structure calculations [35,50,72]. In Sec. III A 2, the experimental $A_{el}^{exp}[^3P_1^0]$ value was used to accordingly shift the resulting $B_{el}[^1P_1^0]$ values from all three approximations, i.e., SrD, SD, and SDT, that were used in the SrD-SR-MCDHF+RCI calculations. Considering only the $B_{el}[^1P_1^0]$ result from the most extensive SDT calculation and evaluating the difference $B_{el}(SDT) - B_{el}(SDT)^{shifted}$ yields an error estimate of 32 MHz/b. When applying this shift to the final results of the remaining calculations, we acquire three more error bars: 54 MHz/b from the S-MR-MCDHF calculations, 64 MHz/b

from the SrD-MR-MCDHF calculations, and 91 MHz/b from the CI-DFS calculations.

C. Statistical standard deviation

The individual results provided by the four independent sets of calculations could be regarded as a statistical sample and, in that case, the average value μ and the standard deviation σ can be evaluated. For the {622, 693, 717, 778} set of $B_{\text{el}}[{}^1P_1^0]$ values, it is $\mu \pm \sigma = 703 \pm 56$ MHz/b, which places $B_{\text{el}}[{}^1P_1^0]$ between 591 and 815 MHz/b within the 2σ condition (95%). In this manner, we obtain another uncertainty estimate equivalent to 56 MHz.

D. Zinc analogy

In a recent paper [35], the quadrupole moment $Q({}^{67}\text{Zn})$ was evaluated based on 11 independent multiconfiguration calculations of the EFG $\propto B_{\text{el}}$ for the $4s4p\ {}^3P_1^0$ and $4s4p\ {}^3P_2^0$ states in Zn I. The final accuracy of the calculated EFGs was estimated using the scatter of the individual results of these 11 calculations, resulting in a relative error of about 8%. The valence structure of the $4s4p\ {}^3P_{1,2}^0$ states in neutral zinc is quite similar to the structure of the $5s^25p6s\ {}^13P_1^0$ tin states, which are of interest in this work; in both cases, there are two electrons outside the closed shells, and the orbitals of these valence electrons have similar angular symmetries. Thereby, one expects that, for atomic calculations using similar computational approaches, the relative error bars of the computed hyperfine factors will be comparable. Adopting the 8% relative error bar, an uncertainty of 56 MHz/b is inferred for the $B_{\text{el}}[{}^1P_1^0]$ value deduced in this paper.

E. Final accuracy

The considerations above lead to diverse error bars, which, according to the order of their appearance in the text, are (in units of MHz/b): 78, 26, 70, 20, 32, 54, 64, 91, 56, and 56. The largest of these uncertainties, i.e., 91 MHz/b, places $B_{\text{el}}[{}^1P_1^0]$ between 521 and 885 MHz/b within the 2σ condition, which is a rather conservative choice. On the other hand, the smallest of all these error estimates, i.e., 20 MHz/b, positions $B_{\text{el}}[{}^1P_1^0]$ between 663 and 743 MHz/b within the 2σ condition. This interval does not overlap with all individual $B_{\text{el}}[{}^1P_1^0]$ values resulting from the four independent sets of calculations and, therefore, such an error bar is not appropriate. Assuming that some of the obtained error bars possibly overestimate the uncertainty in our concluding $B_{\text{el}}[{}^1P_1^0]$ value, and that a few others might underestimate it, the rounded value of 50 MHz/b is a reasonable choice. The final result of this paper, then, becomes

$$B_{\text{el}}[{}^1P_1^0] = 703 \pm 50 \text{ MHz/b}, \quad (20)$$

localizing $B_{\text{el}}[{}^1P_1^0]$ between 603 and 803 MHz/b with 95% confidence.

Recent calculations performed in [73] based on Fock-space coupled-cluster theory resulted in a slightly smaller value of $B_{\text{el}}[{}^1P_1^0] = 645(58)$ MHz/b, lying within our error bars. The only other available value is the one given by Eberz *et al.* [74], i.e., $B_{\text{el}}[{}^1P_1^0] = 593$ MHz/b, which is approximately 15% smaller than the result of this work. It is, therefore, seen that

the recent rigorous reinvestigations of the hyperfine electronic factors of excited states in Sn I yield, independently of the method used, $B_{\text{el}}[{}^1P_1^0]$ values, which are larger than the initially computed value a few decades ago.

V. QUADRUPOLE MOMENTS

The computed $B_{\text{el}}[{}^1P_1^0]$ value can be used to deduce the nuclear quadrupole moments $Q({}^A\text{Sn}) = B/B_{\text{el}}$ of the tin isotopes for which the E2 hyperfine constant B was measured. The $B_{\text{el}}[{}^1P_1^0]$ value resulting from the present multiconfiguration calculations was recently employed by Yordanov *et al.* [12] to extract the nuclear quadrupole moments of odd- A tin isotopes. As mentioned in the Introduction, the final $B_{\text{el}} \propto$ EFG value for the $5s^25p6s\ {}^1P_1^0$ state has been slightly shifted from 706(50) MHz/b that was reported and used in Ref. [12] to 703(50) MHz/b in this paper. The Q values listed in the last column of Table 1 in Ref. [12] should, therefore, be increased by a tiny factor of 706/703.

For a few tin isotopes, more than one experimental value of E2 hyperfine constants is available, allowing us to compare the extracted quadrupole moments. The E2 hyperfine constant $B[{}^1P_1^0]$ for the $I = 5/2$ state of ${}^{109}\text{Sn}$ was measured independently in Refs. [12,74], and their results are, respectively, $B[{}^1P_1^0] = 212.0(27.0)$ MHz and $B[{}^1P_1^0] = 154(5)$ MHz. In Ref. [74], the computed $B_{\text{el}}[{}^1P_1^0] = 593$ MHz/b value is also available, despite the fact that they used the data related to the ${}^3P_1^0$ state, i.e., $B[{}^3P_1^0] = -43.0(12.0)$ MHz and $B_{\text{el}}[{}^3P_1^0] = -138$ MHz/b, to extract the quadrupole moment $Q({}^{109}\text{Sn}) = 310(100)$ mb. By combining the experimental $B[{}^1P_1^0]$ result of Ref. [12] with the presently computed $B_{\text{el}}[{}^1P_1^0] = 703(50)$, we obtain $Q({}^{109}\text{Sn}) = 219(7)(16)$, which significantly differs from the above-mentioned value of $Q({}^{109}\text{Sn}) = 310(100)$ mb. These two quadrupole moments merely overlap with each other due to the large uncertainty of 100 mb in the latter value. Further, the $B_{\text{el}}[{}^1P_1^0]$ value given in Ref. [74] barely overlaps with the present $B_{\text{el}}[{}^1P_1^0]$ value, which strengthens the need to improve the accuracy of the electronic hyperfine factors.

Finally, taking the ${}^{119}\text{Sn}$ isotope as an example, we propose

$$Q({}^{119}\text{Sn}) = -0.176(4)(12) \text{ b}, \quad (21)$$

where (12) represents the theoretical uncertainty of 7% of the $B_{\text{el}}[{}^1P_1^0]$ deduced in this work and (4) represents the experimental uncertainty of the measured $B[{}^1P_1^0]$ in Ref. [12]. We notice that the theoretical uncertainty suggested above is about three times larger than the experimental uncertainty. In the previous section, a number of considerations were taken into account to provide a well-grounded estimate of the theoretical uncertainties in our final $B_{\text{el}}[{}^1P_1^0]$ value. Nonetheless, one should always remain cautious toward error estimates of electronic hyperfine factors deduced from atomic calculations and of the corresponding error bars in the evaluated nuclear quadrupole moments Q . The element bismuth is a good example of the difficulties in estimating such error bars. Table I in Ref. [56] lists the proposed values of the nuclear quadrupole moment Q for the ${}^{209}\text{Bi}$ isotope. The error bars of several of those values not only do not overlap, but they do not even touch each other (to make all of the error bars overlap, the relative uncertainties would have to exceed 50%). We should, however, also note here that the valence structure of the tin

atom is less complicated and less demanding computationally than the valence structure of the bismuth atom, and we are confident enough that the deduced error bars in this paper are trustworthy.

VI. CONCLUSIONS

We presented the details of the theoretical calculations of the isotope-independent E2 hyperfine factor B_{el} (\propto EFG), which was recently used to extract nuclear quadrupole moments Q of tin isotopes [12]. Four independent computational approaches were employed to finally provide the value of $B_{el} = 703(50)$ MHz/b for the $5s^25p6s\ ^1P_1^o$ excited state of Sn I. Three of these approaches were based on the MCDHF-RCI method as implemented in the GRASP packages, while the fourth approach relied on the CI-DFS theory. The convergence of the $B_{el}[\ ^1P_1^o]$ values was monitored as the CSF expansions were enlarged by allowing single, double, and, depending on the correlation model, also triple electron substitutions from the reference configuration(s). Efforts were made to provide a realistic theoretical uncertainty for the final $B_{el}[\ ^1P_1^o]$ value by accounting for statistical principles, the correlation with the isotope-independent M1 hyperfine factor A_{el} , and previous calculations of electronic hyperfine factors on systems with electronic structure similar to that of Sn I.

The deduced relative accuracy of the present atomic *ab initio* calculations of the EFG is of the order of 7%, leading to even larger uncertainties in the extracted $Q(\text{Sn})$ values due to the uncertainty in the measured B . This level of accuracy is certainly inferior to the deduced $Q(\text{Sn})$ values from the solid-state density functional calculations performed by Barone *et al.* [75], which are about an order of magnitude more accurate. In general, the accuracy of the atomic *ab initio* calculations of EFGs strongly depends on the valence structure of the atom, or ion, in question. We should note that, in the extreme case of lithiumlike systems, the relative uncertainties of the atomic calculations of hyperfine structures can be limited to 0.001%–0.01% [58,59,76–81]. Even though the tin atom is far more demanding computationally than the lithiumlike systems, an atomic calculation of hyperfine structures with lower uncertainty would be possible for singly ionized tin, with one electron outside closed shells, and it would be even more accurate, for triply ionized tin, which has one electron outside the $n < 5$ core. Such calculations, as the latter, would likely challenge the accuracy of the solid-state methods. We hereby encourage experimentalists to consider one, or both, of the above-mentioned ions.

Interestingly, we observe that all computed $A_{el}[\ ^3P_1^o]$ values are smaller than the experimental $A_{el}^{\text{exp}}[\ ^3P_1^o] = 2398$ MHz/ μ_N value, independently of the computational method, or the correlation model. This could be explained by the lack of variational freedom intrinsic to the layer-by-layer optimization strategy, which hinders the contraction of spectroscopic orbitals when core-valence correlation is accounted for. In the specific case of Sn I, the spectroscopic $4d$ soft shell, i.e., lying between the core and the valence orbitals, is expected to be highly sensitive to core-valence correlation that might not be effectively captured. Natural orbitals were recently used, as an efficient tool to overcome the limitation of the layer-by-layer optimization scheme, to estimate hyperfine

structure constants in Na I. Thanks to the radial reorganization of the orbitals, the spectroscopic orbitals are ultimately contracted, which affects both M1 and E2 electronic hyperfine factors [72]. Further investigations on the usefulness of the natural orbitals in the calculations of hyperfine structures are in progress.

ACKNOWLEDGMENTS

S.S. is a FRIA grantee of the F.R.S-FNRS Fonds de la Recherche Scientifique (FNRS). M.G. acknowledges support from the FWO & FNRS Excellence of Science Programme (EOS-O022818F), P.J. acknowledges support from the Swedish Research Council (VR) under Contract No. 2015-04842, and I.I.T. acknowledges support by the RFBR Grant No. 18-03-01220.

APPENDIX: SENSITIVITY OF THE HYPERFINE FACTORS AND STABILITY OF THE B_{el} RATIO

As shown in Table V, where the influence of the choice of the CSF expansion and the orbital basis was investigated, the $A_{el}[\ ^1P_1^o]/A_{el}[\ ^3P_1^o]$ ratio displays a much higher sensitivity in comparison to the $B_{el}[\ ^3P_1^o]/B_{el}[\ ^1P_1^o]$ ratio. Also according to Table V, the computed $A_{el}[\ ^3P_1^o]$ values range from 2161 to 2303 MHz/ μ_N (6%–7%). Hence, the sensitivity of the $A_{el}[\ ^1P_1^o]/A_{el}[\ ^3P_1^o]$ ratio, which takes values from 0.124 to 0.185 (30%–50%), must arise from the computed $A_{el}[\ ^1P_1^o]$ values.

The extreme sensitivity of $A_{el}[\ ^1P_1^o]$ to correlation models is not really surprising if one performs calculations using the quasirelativistic Hartree-Fock and Breit-Pauli [47] method in the single-configuration approximation. In the Breit-Pauli (BP) scheme, the low value of the ratio $A_{el}[\ ^1P_1^o]/A_{el}[\ ^3P_1^o]$ can indeed be understood. The A_{el} value of the *pure* $\ ^3P_1^o$, i.e., without considering any relativistic *LS*-term mixing, arises from the addition of the three contributions [82] (orbital, spin-dipole, and contact term), which interfere positively. On the other hand, the A_{el} value of the *pure* $\ ^1P_1^o$ is only made of a (larger) orbital contribution, the total spin value ($S = 0$) forbidding the two other contributions. For $J = 1$, the two singlet and triplet symmetries are mixed with relative phases that result from the orthogonality constraints. The eigenvector dominated by the triplet character has the same signs of both components, which makes the $A_{el}[\ ^3P_1^o]$ value even larger than the one of the pure triplet (increase of 40%). For the state dominated by the singlet, strong cancellation occurs due to the triplet contamination, reducing the $A_{el}[\ ^1P_1^o]$ value by 61%. Strong cancellation in the estimation of a property usually involves high uncertainty.

The “sharing rule” [83,84] that is used to quantify configuration mixing from the measured isotope shifts can be applied to the term-mixing analysis of the B_{el} . In the single-configuration approximation, the ratio $B_{el}[\ ^3P_1^o]/B_{el}[\ ^1P_1^o]$ is exactly $-\frac{1}{2} = -0.5$, resulting from angular momentum algebra, when using the same orbital sets for describing both levels. Assuming a simple $\ ^3P^o - \ ^1P^o$ mixing for $J = 1$, we have

$$\begin{aligned}\Psi(\text{“} \ ^3P_1^o \text{”}) &= a|\ ^3P_1^o\rangle + b|\ ^1P_1^o\rangle, \\ \Psi(\text{“} \ ^1P_1^o \text{”}) &= b|\ ^3P_1^o\rangle - a|\ ^1P_1^o\rangle,\end{aligned}\tag{A1}$$

where $|^{1,3}P_1^0\rangle$ are the two lowest $J^\Pi = 1^-$ states resulting from pure LS terms and $\Psi(^{1,3}P_1^0)$ are the corresponding mixed states. Using the analytical ratio $B_{\text{el}}[{}^1P_1^0]/B_{\text{el}}[{}^3P_1^0] = -2$, one can estimate

$$\begin{aligned} B_{\text{el}}[{}^3P_1^0] &= B_{\text{el}}[{}^3P_1^0](a^2 - 2b^2), \\ B_{\text{el}}[{}^1P_1^0] &= B_{\text{el}}[{}^3P_1^0](b^2 - 2a^2), \end{aligned} \quad (\text{A2})$$

from which we deduce

$$R = B_{\text{el}}[{}^3P_1^0]/B_{\text{el}}[{}^1P_1^0] = \frac{a^2 - 2b^2}{b^2 - 2a^2}. \quad (\text{A3})$$

Adopting for this ratio a reasonable guess that is guided by the experimental result from Ref. [12] and that offers numerical simplicity, $R = -\frac{1}{4}$, one gets the following analytical eigenvector compositions:

$$\begin{aligned} \Psi(^{3}P_1^0) &= \frac{\sqrt{7}}{3} |{}^3P_1^0\rangle + \frac{\sqrt{2}}{3} |{}^1P_1^0\rangle, \\ \Psi(^{1}P_1^0) &= \frac{\sqrt{2}}{3} |{}^3P_1^0\rangle - \frac{\sqrt{7}}{3} |{}^1P_1^0\rangle. \end{aligned} \quad (\text{A4})$$

In other terms, the ratio $B_{\text{el}}[{}^3P_1^0]/B_{\text{el}}[{}^1P_1^0]$ only reflects the singlet-triplet mixing in this simple model. We should not be surprised by its relative stability when more elaborate models are used. Extracting the 3P_0 character (a^2) from the lowest (${}^3P_1^0$) BP eigenvector obtained in a simple MR model mixing the $\{5s^25p6s, 5s5p5d6s, 5p^36s\}$ configurations, we get after renormalization $a^2 = 0.77617$ from which we determine $B_{\text{el}}[{}^3P_1^0]/B_{\text{el}}[{}^1P_1^0] = -0.247$ according to

$$B_{\text{el}}[{}^3P_1^0]/B_{\text{el}}[{}^1P_1^0] = \frac{a^2 - 2b^2}{b^2 - 2a^2} = -\frac{3a^2 - 2}{3a^2 - 1}. \quad (\text{A5})$$

For the other BP eigenvector (${}^1P_1^0$), we have $a^2 = 0.77641$ from which one confirms the ratio $B_{\text{el}}[{}^3P_1^0]/B_{\text{el}}[{}^1P_1^0] = -0.248$. The latter value is not too far from the above $R = -\frac{1}{4}$ ratio value that would be obtained from the hypothetical ($a^2 = \frac{7}{9}$; $b^2 = \frac{2}{9}$) singlet-triplet mixing, taking into account that (i) one trusts the nonrelativistic ratio $B_{\text{el}}[{}^3P_1^0]/B_{\text{el}}[{}^1P_1^0] = -\frac{1}{2}$ of the single-configuration approximation, (ii) the BP eigenvector has to be renormalized, and (iii) one assumes no contamination by other LS symmetries (${}^3D_1^0, {}^5P_1^0, {}^5D_1^0, {}^5F_1^0, {}^7D_1^0, \dots, {}^{25}X_1^0$).

-
- [1] C. Froese Fischer, G. Gaigalas, P. Jönsson, and J. Bieroń, *Comput. Phys. Commun.* **237**, 184 (2019).
- [2] E. Kahl and J. Berengut, *Comput. Phys. Commun.* **238**, 232 (2019).
- [3] M. G. Kozlov, S. G. Porsev, M. S. Safronova, and I. I. Tupitsyn, *Comput. Phys. Commun.* **195**, 199 (2015).
- [4] A. Hibbert, *Phys. Scr.* **2004**, 39 (2004).
- [5] M. S. Safronova, D. Budker, D. DeMille, D. F. Jackson Kimball, A. Derevianko, and C. W. Clark, *Rev. Mod. Phys.* **90**, 025008 (2018).
- [6] K. Wang, C. X. Song, P. Jönsson, G. D. Zanna, S. Schiffmann, M. Godefroid, G. Gaigalas, X. H. Zhao, R. Si, C. Y. Chen, and J. Yan, *Astrophys. J., Suppl. Ser.* **239**, 30 (2018).
- [7] J. Ekman, P. Jönsson, S. Gustafsson, H. Hartman, G. Gaigalas, M. R. Godefroid, and C. Froese Fischer, *Astron. Astrophys.* **564**, A24 (2014).
- [8] L. Filippin, R. Beerwerth, J. Ekman, S. Fritzsche, M. Godefroid, and P. Jönsson, *Phys. Rev. A* **94**, 062508 (2016).
- [9] V. A. Dzuba, J. C. Berengut, C. Harabati, and V. V. Flambaum, *Phys. Rev. A* **95**, 012503 (2017).
- [10] S. Verdebout, C. Nazé, P. Jönsson, P. Rynkun, M. Godefroid, and G. Gaigalas, *At. Data Nucl. Data Tables* **100**, 1111 (2014).
- [11] M. G. Kozlov, M. S. Safronova, J. R. Crespo López-Urrutia, and P. O. Schmidt, *Rev. Mod. Phys.* **90**, 045005 (2018).
- [12] D. T. Yordanov, L. V. Rodriguez, D. L. Balabanski, J. Bieroń, M. L. Bissell, K. Blaum, B. Cheal, J. Ekman, G. Gaigalas, R. F. Garcia Ruiz, G. Georgiev, W. Gins, M. R. Godefroid, C. Gorges, Z. Harman, H. Heylen, P. Jönsson, A. Kanellakopoulos, S. Kaufmann, C. H. Keitel, V. Lagaki, S. Lechner *et al.*, *Commun. Phys.* **3**, 107 (2020).
- [13] N. Frömmgen, D. L. Balabanski, M. L. Bissell, J. Bieroń, K. Blaum, B. Cheal, K. Flanagan, S. Fritzsche, C. Geppert, M. Hammen, M. Kowalska, K. Kreim, A. Krieger, R. Neugart, G. Neyens, M. M. Rajabali, W. Nörtershäuser, J. Papuga, and D. T. Yordanov, *Eur. Phys. J. D* **69**, 164 (2015).
- [14] D. T. Yordanov, D. L. Balabanski, J. Bieroń, M. L. Bissell, K. Blaum, I. Budinčević, S. Fritzsche, N. Frömmgen, G. Georgiev, C. Geppert, M. Hammen, M. Kowalska, K. Kreim, A. Krieger, R. Neugart, W. Nörtershäuser, J. Papuga, and S. Schmidt, *Phys. Rev. Lett.* **110**, 192501 (2013).
- [15] C. Wraith, X. F. Yang, L. Xie, C. Babcock, J. Biero, J. Billowes, M. L. Bissell, K. Blaum, B. Cheal, L. Filippin, R. F. G. Ruiz, W. Gins, L. K. Grob, G. Gaigalas, M. Godefroid, C. Gorges, H. Heylen, M. Honma, P. Jönsson, S. Kaufmann *et al.*, *Phys. Lett. B* **771**, 385 (2017).
- [16] A. Antognini, N. Berger, T. E. Cocolios, R. Dressler, R. Eichler, A. Eggenberger, P. Indelicato, K. Jungmann, C. H. Keitel, K. Kirch, A. Knecht, N. Michel, J. Nuber, N. S. Oreshkina, A. Ouf, A. Papa, R. Pohl, M. Pospelov, E. Rapisarda, N. Ritjoho *et al.*, *Phys. Rev. C* **101**, 054313 (2020).
- [17] M. Cohen and F. Reif, in *Solid State Physics Series, Volume 5*, edited by F. Seitz and D. Turnbull (Academic, New York, 1957), pp. 321–438.
- [18] P. Schwerdtfeger, M. Pernpointner, and W. Nazarewicz, in *Calculation of NMR and EPR Parameters. Theory and Applications*, edited by M. Kaupp, M. Bühl, and V. G. Malkin (Wiley, Weinheim, 2004), pp. 279–291.
- [19] E. A. C. Lucken, *Nuclear Quadrupole Coupling Constants* (Academic, London, 1969).
- [20] T. Das and E. Hahn, *Solid State Physics: Supplement I: Nuclear Quadrupole Resonance Spectroscopy* (Academic, New York, 1958).
- [21] *Mössbauer Spectroscopy*, edited by D. Dickson and F. Berry (Cambridge University Press, Cambridge, 2005).
- [22] Y. Chen and D. Yang, *Mössbauer Effect in Lattice Dynamics: Experimental Techniques and Applications* (Wiley, Hoboken, NJ, 2007).
- [23] H. Haas and D. A. Shirley, *J. Chem. Phys.* **58**, 3339 (1973).
- [24] H. Haas, S. P. A. Sauer, L. Hemmingsen, V. Kellö, and P. W. Zhao, *Europhys. Lett.* **117**, 62001 (2017).

- [25] P. Raghavan, *At. Data Nucl. Data Tables* **42**, 189 (1989).
- [26] N. J. Stone, *At. Data Nucl. Data Tables* **111-112**, 1 (2016).
- [27] P. Pyykkö, *Mol. Phys.* **116**, 1328 (2018).
- [28] I. P. Grant, *Relativistic Quantum Theory of Atoms and Molecules: Theory and Computation* (Springer, New York, 2007).
- [29] C. Froese Fischer, M. Godefroid, T. Brage, P. Jönsson, and G. Gaigalas, *J. Phys. B: At., Mol. Opt. Phys.* **49**, 182004 (2016).
- [30] I. I. Tupitsyn and A. V. Loginov, *Opt. Spectrosc.* **94**, 319 (2003).
- [31] I. I. Tupitsyn, V. M. Shabaev, J. R. Crespo López-Urrutia, I. Draganić, R. S. Orts, and J. Ullrich, *Phys. Rev. A* **68**, 022511 (2003).
- [32] I. I. Tupitsyn, A. V. Volotka, D. A. Glazov, V. M. Shabaev, G. Plunien, J. R. Crespo López-Urrutia, A. Lapierre, and J. Ullrich, *Phys. Rev. A* **72**, 062503 (2005).
- [33] R. Soria Orts, Z. Harman, J. R. Crespo López-Urrutia, A. N. Artemyev, H. Bruhns, A. J. González Martínez, U. D. Jentschura, C. H. Keitel, A. Lapierre, V. Mironov, V. M. Shabaev, H. Tawara, I. I. Tupitsyn, J. Ullrich, and A. V. Volotka, *Phys. Rev. Lett.* **97**, 103002 (2006).
- [34] I. Tupitsyn, Dirac-Fock-Sturm method in relativistic calculations for atoms and two-atomic molecules, Ph.D. thesis, Saint-Petersburg State University, Saint-Petersburg, 2008 (in Russian).
- [35] J. Bieroń, L. Filippin, G. Gaigalas, M. Godefroid, P. Jönsson, and P. Pyykkö, *Phys. Rev. A* **97**, 062505 (2018).
- [36] P. Jönsson, G. Gaigalas, J. Bieroń, C. Froese Fischer, and I. P. Grant, *Comput. Phys. Commun.* **184**, 2197 (2013).
- [37] I. P. Grant, B. J. McKenzie, P. H. Norrington, D. F. Mayers, and N. C. Pyper, *Comput. Phys. Commun.* **21**, 207 (1980).
- [38] G. Gaigalas, Z. Rudzikas, and C. Froese Fischer, *J. Phys. B: At., Mol. Opt. Phys.* **30**, 3747 (1997).
- [39] G. Gaigalas, S. Fritzsche, and I. P. Grant, *Comput. Phys. Commun.* **139**, 263 (2001).
- [40] I. P. Grant and N. C. Pyper, *J. Phys. B: At. Mol. Phys.* **9**, 761 (1976).
- [41] C. Y. Zhang, K. Wang, M. Godefroid, P. Jönsson, R. Si, and C. Y. Chen, *Phys. Rev. A* **101**, 032509 (2020).
- [42] I. Lindgren and A. Rosén, *Case Stud. At. Phys.* **4**, 93 (1974).
- [43] P. Jönsson, F. Parpia, and C. Froese Fischer, *Comput. Phys. Commun.* **96**, 301 (1996).
- [44] A. Edmonds, *Angular Momentum in Quantum Mechanics* (Princeton University Press, Princeton, New Jersey, 1957).
- [45] A. E. Barzakh, D. Atanasov, A. N. Andreyev, M. Al Monthery, N. A. Althubiti, B. Andel, S. Antalic, K. Blaum, T. E. Cocolios, J. G. Cubiss, P. Van Duppen, T. D. Goodacre, A. de Roubin, Y. A. Demidov, G. J. Farooq-Smith, D. V. Fedorov, V. N. Fedosseev, D. A. Fink, L. P. Gaffney, L. Ghys *et al.*, *Phys. Rev. C* **101**, 034308 (2020).
- [46] P. Pyykkö and M. Seth, *Theor. Chem. Acc.* **96**, 92 (1997).
- [47] C. Froese Fischer, T. Brage, and P. Jönsson, *Computational Atomic Structure. An MCHF Approach* (Institute of Physics Publishing, Bristol, 1997).
- [48] S. Verdebout, P. Rynkun, P. Jönsson, G. Gaigalas, C. Froese Fischer, and M. Godefroid, *J. Phys. B: At., Mol. Opt. Phys.* **46**, 085003 (2013).
- [49] J. Dembczyński and H. Rebel, *Phys. B+C (Amsterdam)* **125**, 341 (1984).
- [50] J. Bieroń, C. Froese Fischer, P. Indelicato, P. Jönsson, and P. Pyykkö, *Phys. Rev. A* **79**, 052502 (2009).
- [51] B. Engels, *Theor. Chim. Acta* **86**, 429 (1993).
- [52] B. Engels, L. A. Eriksson, and S. Lunell, *Adv. Quantum Chem.* **27**, 297 (1996).
- [53] P. Jönsson, A. Ynnerman, C. Froese Fischer, M. R. Godefroid, and J. Olsen, *Phys. Rev. A* **53**, 4021 (1996).
- [54] M. R. Godefroid, G. Van Meulebeke, P. Jönsson, and C. Froese Fischer, *Z. Phys. D-Atoms, Molecules Clusters* **42**, 193 (1997).
- [55] J. Bieroń, C. Froese Fischer, P. Jönsson, and P. Pyykkö, *J. Phys. B: At., Mol. Opt. Phys.* **41**, 115002 (2008).
- [56] J. Bieroń and P. Pyykkö, *Phys. Rev. Lett.* **87**, 133003 (2001).
- [57] J. Bieroń, P. Pyykkö, and P. Jönsson, *Phys. Rev. A* **71**, 012502 (2005).
- [58] J. Bieroń, P. Jönsson, and C. Froese Fischer, *Phys. Rev. A* **60**, 3547 (1999).
- [59] J. Bieroń, P. Jönsson, and C. Froese Fischer, *Phys. Rev. A* **53**, 2181 (1996).
- [60] W. R. Johnson, *Atomic Structure Theory: Lectures on Atomic Physics* (Springer, Berlin, 2007).
- [61] D. Sundholm and J. Olsen, *Phys. Rev. A* **47**, 2672 (1993).
- [62] A. Kramida, Yu. Ralchenko, J. Reader, and NIST ASD Team, NIST Atomic Spectra Database (version 5.7.1) (online), National Institute of Standards and Technology, Gaithersburg, MD. Available at <https://physics.nist.gov/asd>.
- [63] W. Brill, The Arc Spectrum of Tin, Ph.D. thesis, Purdue University, Lafayette, IN, 1964.
- [64] T. Carette, C. Drag, O. Scharf, C. Blondel, C. Delsart, C. Froese Fischer, and M. Godefroid, *Phys. Rev. A* **81**, 042522 (2010).
- [65] J. Li, P. Jönsson, M. Godefroid, C. Dong, and G. Gaigalas, *Phys. Rev. A* **86**, 052523 (2012).
- [66] G. Gaigalas, P. Rynkun, L. Radžiūtė, D. Kato, M. Tanaka, and P. Jönsson, *Astrophys. J., Suppl. Ser.* **248**, 13 (2020).
- [67] N. Michel, N. S. Oreshkina, and C. H. Keitel, *Phys. Rev. A* **96**, 032510 (2017).
- [68] K. Koch, K. Koepf, D. Van Neck, H. Rosner, and S. Cottenier, *Phys. Rev. A* **81**, 032507 (2010).
- [69] M. S. Safronova and W. R. Johnson, *Adv. At. Mol. Opt. Phys.* **55**, 191 (2008).
- [70] M. S. Safronova and U. I. Safronova, *Phys. Rev. A* **83**, 052508 (2011).
- [71] H.-K. Chung, B. J. Braams, K. Bartschat, A. G. Császár, G. W. F. Drake, T. Kirchner, V. Kokoouline, and J. Tennyson, *J. Phys. D: Appl. Phys.* **49**, 363002 (2016).
- [72] S. Schiffmann, M. Godefroid, J. Ekman, P. Jönsson, and C. F. Fischer, *Phys. Rev. A* **101**, 062510 (2020).
- [73] F. P. Gustafsson, C. M. Ricketts, M. L. Reitsma, R. F. Garcia Ruiz, S. W. Bai, J. C. Berengut, J. Billowes, C. L. Binnersley, A. Borschevsky, T. E. Cocolios, B. S. Cooper, R. P. de Groote, K. T. Flanagan, A. Koszorús, G. Neyens, H. A. Perrett, A. R. Vernon, Q. Wang, S. G. Wilkins, and X. F. Yang, *Phys. Rev. A* **102**, 052812 (2020).
- [74] J. Eberz, U. Dinger, G. Huber, H. Lochmann, R. Menges, G. Ulm, R. Kirchner, O. Klepper, T. Kühn, and D. Marx, *Z. Phys. A* **326**, 121 (1987).
- [75] G. Barone, R. Mastalerz, M. Reiher, and R. Lindh, *J. Phys. Chem. A* **112**, 1666 (2008).

- [76] M. Tong, P. Jönsson, and C. Froese Fischer, *Phys. Scr.* **48**, 446 (1993).
- [77] Z.-C. Yan, D. K. McKenzie, and G. W. F. Drake, *Phys. Rev. A* **54**, 1322 (1996).
- [78] V. A. Yerokhin, *Phys. Rev. A* **77**, 020501(R) (2008).
- [79] V. A. Yerokhin, *Phys. Rev. A* **78**, 012513 (2008).
- [80] E. Y. Korzinin, N. S. Oreshkina, and V. M. Shabaev, *Phys. Scr.* **71**, 464 (2005).
- [81] N. S. Oreshkina, A. V. Volotka, D. A. Glazov, I. I. Tupitsyn, V. M. Shabaev, and G. Plunien, *Optics Spectro.* **102**, 815 (2007).
- [82] P. Jönsson, C.-G. Wahlström, and C. F. Fischer, *Comput. Phys. Commun.* **74**, 399 (1993).
- [83] J. Bauche and R.-J. Champeau, *Adv. At. Mol. Phys.* **12**, 39 (1976).
- [84] Y. Ishida, H. Iimura, S. Ichikawa, and T. Horiguchi, *J. Phys. B: At., Mol. Opt. Phys.* **30**, 2569 (1997).